Structure of ^{28}Mg and influence of the neutron pf shell

J. Williams, G. C. Ball, A. Chester, T. Domingo, A. B. Garnsworthy, G. Hackman, J. Henderson, R. Henderson, R. Krücken, Anil Kumar, K. D. Launey, J. Measures, O. Paetkau, J. Park, G. H. Sargsyan, J. Smallcombe, P. C. Srivastava, K. Starosta, C. E. Svensson, K. Whitmore, and M. Williams

Phys. Rev. C **100**, 014322 — Published 29 July 2019

DOI: 10.1103/PhysRevC.100.014322

Structure of ^{28}Mg and influence of the neutron pf shell

J. Williams,[1,*] G. C. Ball,[2] A. Chester,[1] T. Domingo,[1] A. B. Garnsworthy,[2] G. Hackman,[2] J. Henderson,[2] R. Henderson,[2] R. Krücken,[2,3] A. Kumar,[4] K. D. Launey,[5] J. Measures,[2,6] O. Paetkau,[2] J. Park,[2,3] G. H. Sargsyan,[5] J. Smallcombe,[2] P. C. Srivastava,[4] K. Starosta,[1,†] C. E. Svensson,[7] K. Whitmore,[1] and M. Williams[2]

[1]*Department of Chemistry, Simon Fraser University, 8888 University Drive, Burnaby, British Columbia, Canada V5A 1S6*
[2]*TRIUMF, 4004 Wesbrook Mall, Vancouver, British Columbia, Canada V6T 2A3*
[3]*Department of Physics & Astronomy, University of British Columbia, Vancouver, British Columbia, Canada V6T 1Z4*
[4]*Department of Physics, Indian Institute of Technology Roorkee, Roorkee, Uttarakhand, India 247667*
[5]*Department of Physics & Astronomy, Louisiana State University, Baton Rouge, Louisiana, USA 70803*
[6]*Department of Physics, University of Surrey, Guildford, Surrey, United Kingdom GU2 7XH*
[7]*Department of Physics, University of Guelph, Guelph, Ontario, Canada N1G 2W1*

(Dated: July 9, 2019)

Gamma-ray spectroscopy and lifetime measurements using the Doppler Shift Attenuation Method (DSAM) were performed on the nucleus ^{28}Mg near the $N = 20$ 'island of inversion', which was populated using a ^{12}C(^{18}O,2p)^{28}Mg fusion-evaporation reaction to investigate the impact of shell evolution on its high-lying structure. Three new levels were identified at 7203(3), 7747(2), and 7929.3(12) keV along with several new gamma rays. A newly extracted B(E2; $4_1^+ \rightarrow 2_1^+$) of 42(7) e^2fm^4 indicates reduced collectivity in the yrast band at high spin, consistent with *ab initio* SA-NCSM calculations. At high excitation energy, evidence for the population of intruder orbitals was obtained through identification of negative parity levels ($I^\pi = (0,4)^-$, $(4,5)^-$). Calculations using the SDPF-MU interaction indicate that these levels arise from single neutron excitation to the pf shell and provides evidence for the lowering of these intruder orbitals approaching the 'island of inversion'.

I. INTRODUCTION

The existence of an 'island of inversion' (IoI) centred on neutron-rich Na and Mg, is well established [1]. This IoI is defined by the ground state population of neutrons in the pf-shell due to the collapse of the $N = 20$ shell gap resulting from the influence of nucleon-nucleon interactions and nuclear deformation [2, 3]. The $N = 20$ IoI is one of many regions of neutron shell breaking, with recent evidence suggesting that the neutron rich side of the $N = 20$ IoI merges with the $N = 28$ IoI for Mg isotopes [4]. In addition to investigating the boundaries of the IoI, recent experiments have studied shell evolution in Na and Mg isotopes approaching the IoI [5–8]. Determining the onset of the IoI requires the identification and investigation of intruder orbitals as a function of neutron excess. At lower neutron numbers ($N < 20$), population of these intruder orbitals is found at levels with high excitation energy. The present work investigates the $N = 16$ nucleus ^{28}Mg, for which data on these high-lying levels is scarce.

In the case of ^{28}Mg, which lies halfway between $N = Z$ ^{24}Mg and the IoI at ^{32}Mg, shell model calculations in the *sd*-shell are able to reproduce the level energies of low lying states with reasonable accuracy [9]. Recently, developments in *ab initio* models such as the symmetry adapted no-core shell model (SA-NCSM) [10] allow for a detailed probe of the wavefunctions of *sd* shell nuclei without the use of effective charges - an approach which is useful for describing low-lying states in ^{28}Mg where nucleons are expected to primarily occupy the *sd* shell. Additionally, phenomenological models in the *sdpf* shell such as SDPF-U [11] and SDPF-MU [12] have been developed which are capable of probing negative parity states arising from neutron excitation to intruder orbitals in the vicinity of the IoI, as well as the evolution of effective single particle energies in this region.

Although the progress made in both *ab initio* and phenomenological theories is ongoing, experimental data for ^{28}Mg is mostly limited to the low-lying structure. Even for low-lying levels, the existing lifetime measurements often carry large uncertainties. For instance, the two existing measurements of the $4_1^+ \rightarrow 2_1^+$ transition rate in ^{28}Mg disagree significantly [13, 14], leading to opposing conclusions as to the degree of collectivity of states in the yrast band. Furthermore, almost no data exists for states with spin $I > 4$ and/or high excitation energy where the influence of intruder orbitals is expected. Negative parity states in particular provide an explicit indication of intruder orbital occupation. To-date, only one negative parity level ($I^\pi = 3^-$) has been identified in ^{28}Mg, based on angular correlation measurements by Rastegar *et al.* [15]. An $I^\pi = 0^-$ state resulting from the coupling of neutrons in the *sd* and pf shells would be a particularly strong constraint for the single particle energies, due to the limited number of available configurations which couple to zero spin. Shell model calculations have suggested an $I^\pi = 0_1^-$ level below the neutron separation energy of ^{28}Mg [16], but such a state has not been identified by previous experiments.

* ejw1@sfu.ca
† starosta@sfu.ca

In order to investigate the aforementioned concerns, this study employed a ^{12}C(^{18}O,2p)^{28}Mg fusion-evaporation reaction to populate ^{28}Mg with excitation energy up to its neutron separation energy. Transition rates were measured using the Doppler Shift Attenuation Method (DSAM) [17]. These transition rates were used to identify candidates for negative parity states, taking advantage of the known hindrance of E1 transitions compared to Weisskopf estimates seen in the nuclear data from this region [18–20].

II. EXPERIMENTAL DETAILS

The experiment was conducted at the ISAC-II facility at TRIUMF, Canada's particle accelerator centre [21]. Gamma rays from the decay of excited states in ^{28}Mg were detected using the TRIUMF-ISAC gamma-ray escape suppressed spectrometer (TIGRESS) [22], a Compton suppressed high-purity germanium (HPGe) clover array. During the experiment, 13 of the total 16 TIGRESS clover positions were populated in a 4/5/4 configuration, corresponding to full population of detectors at the most upstream and downstream positions within the array. This configuration was chosen to maximize the observation of gamma rays with large Doppler shifts, which improves the sensitivity of the DSAM technique. A 38-element array of CsI(Tl) scintillators, developed as part of the TIGRESS Integrated Plunger (TIP) infrastructure [23], was used for coincident charged particle detection and identification in order to discriminate background events from fusion-evaporation events. The CsI(Tl) array was positioned downstream from the target within the target chamber. The data acquisition system was configured to trigger on events containing at least 2 charged particles in coincidence with at least 2 gamma rays which were not vetoed by the online Compton suppression logic of the TIGRESS DAQ.

The experiment was split into two parts, with the first using a target consisting of a 433 μg/cm^2 carbon layer with a thick 28.79 mg/cm^2 gold backing in order to facilitate lifetime measurements of excited states in ^{28}Mg via the DSAM [24]. The second part used a self-supporting thin target foil of 500 μg/cm^2 diamond-like carbon produced by Micromatter [25] separated from a gold catcher foil positioned 2 mm downstream from the target. The purpose of the thin-target experiment was to obtain increased sensitivity to excited states populated in the reaction via gamma-ray spectroscopy. When using a thin target, the majority of the reaction products emerge from the target and recoil into vacuum prior to de-excitation and gamma-ray emission. Any gamma rays emitted while the reaction residue crosses the gap between the target and catcher in vacuum are detected with a constant Doppler shift, as the residue traverses the gap at constant velocity. Knowing the recoil velocity, the Doppler shift can be corrected for, allowing for true gamma-ray energies to be reconstructed for use in coincidence spectroscopy. The thickness of the gold layer was comparable in both the DSAM and thin targets in order to obtain consistent detection efficiencies in the downstream CsI(Tl) array in both parts of the experiment.

An ^{18}O beam at 48 MeV (2.67 MeV/nucleon) with a rate of $\sim 10^{10}$ particles/s was delivered over a period of 3 days, with the DSAM target running for 40.5 hours and the thin target running for 21 hours. Energy and relative efficiency calibration of the TIGRESS array was performed using standard ^{56}Co and ^{152}Eu sources, with these calibrations extrapolated for gamma rays at higher energy than the 3.451 MeV line in ^{56}Co. Energy calibration of the CsI(Tl) array was performed using a triple-alpha source containing the alpha particle emitters ^{239}Pu, ^{241}Am, and ^{244}Cm.

III. DATA ANALYSIS

Data corresponding to fusion-evaporation were separated from the background using sequential gates on TIGRESS and CsI(Tl) array timing. To reduce contributions from random background coincidences, only events containing 2 CsI(Tl) array hits within 200 ns of each other, 2 TIGRESS hits within 120 ns of each other, and a TIGRESS and a CsI(Tl) array hit within 140 ns of each other were retained. The specific timing windows were chosen based on the observed timing resolution for each detector array used in the experiment. Reaction channel separation was then performed using pulse-shape analysis of waveforms from the CsI(Tl) detector array, as described in Ref. [23]. However, gating on events containing 2 protons was not sufficient by itself to completely isolate ^{28}Mg, as events corresponding to the 2p1n (^{27}Mg), 2p2n (^{26}Mg), 1p (^{29}Al) and 1p1n (^{28}Al) channels remained due to a combination of factors including the lack of neutron detection capability, high reaction cross-sections for population of these contaminant channels, and high beam rate causing a small fraction of events containing one proton to be detected simultaneously as a single event containing two protons. Gamma-gamma coincidences were used in order to further isolate ^{28}Mg, wherein only events containing at least one gamma-ray with energy corresponding to a known gamma-ray in ^{28}Mg were retained (typically the decay of the first excited state, with gamma-ray energy 1473.54(10) keV [19] was used). Add-back of partial gamma-ray energy deposits in neighbouring HPGe cores was performed when evaluating gamma-ray energies in order to improve the signal-to-noise ratio.

Doppler reconstruction of the thin-target data was performed on an event-by-event basis using the method of Ref. [26], taking into account the incoming beam momentum and the position and energy at which charged particles and gamma rays were detected. As only alpha particle calibration data was available for the CsI(Tl) array, the proton energies detected in the array were approximated as the equivalent alpha particle energies

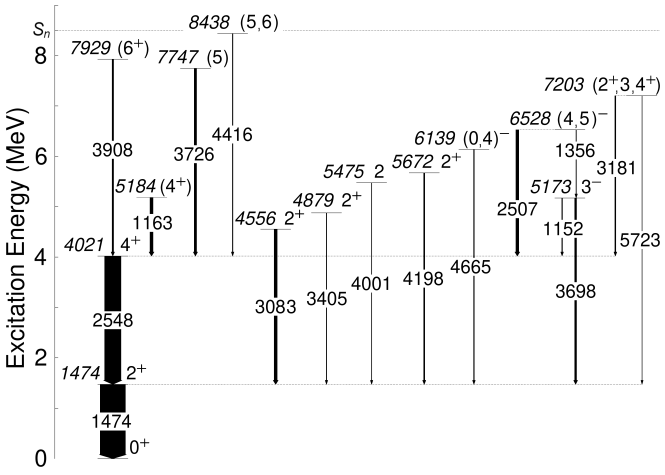

FIG. 1. Scheme of observed levels and gamma rays in ^{28}Mg. Arrow widths specify relative intensities of gamma rays. Spin-parity values are taken from Table III and Ref. [19].

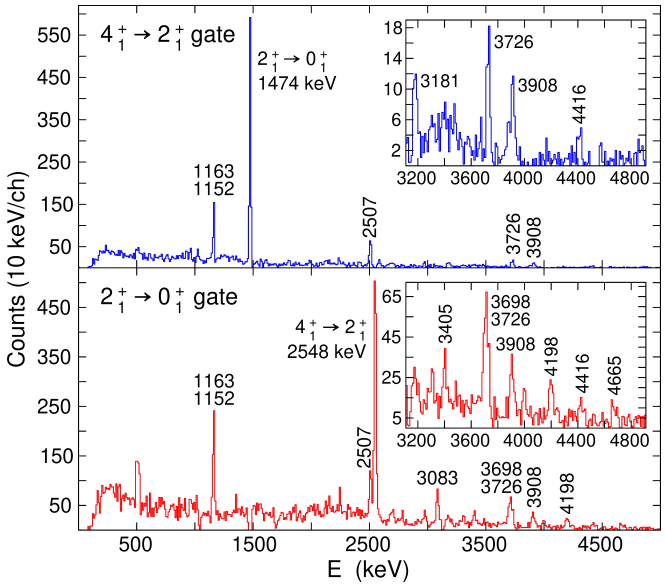

FIG. 2. Background subtracted gamma-ray coincidence spectra showing observed levels in ^{28}Mg, after gating on the $4_1^+ \rightarrow 2_1^+$ transition (top) and the $2_1^+ \rightarrow 0_1^+$ transition (bottom), from Doppler corrected thin target data. Inset figures show the high energy region of the corresponding spectrum.

determined via the triple-alpha source calibration. To improve the energy resolution of the Doppler corrected data, the beam momentum was multiplied by a factor of 0.95 in the calculation to account for slowing of the beam in the target prior to reaction. The Doppler reconstruction procedure generated gamma-ray spectra with typical FWHM-to-position resolution of $\sim 1\%$ (compared to $\sim 0.25\%$ obtained for ^{56}Co calibration source data). The increased peak width in the reconstructed data corresponds to a distribution of recoil velocities due to reaction kinematics, slowing of the residual nucleus in the thin carbon reaction target, as well as the finite size of individual detectors in the CsI and TIGRESS arrays.

Gamma-ray cascades in ^{28}Mg were identified by gating on known gamma rays in ^{28}Mg and projecting out spectra of gamma rays in coincidence. Overall, 17 transitions were identified, corresponding to 14 excited levels in ^{28}Mg. Of these, 8 gamma rays and 3 levels were newly identified. Relative intensities of gamma rays were derived from the thin target gamma-ray spectra using the efficiency calibration of the TIGRESS array derived from ^{56}Co source data. The level scheme established in this study is shown in Fig. 1. Figure 2 shows gamma-ray coincidence spectra demonstrating the quality of the data and providing evidence for the existence of the identified levels.

A. Lifetime determination

The mean lifetimes $\tau_{\rm mean}$ of observed levels in ^{28}Mg were determined using GEANT4 simulation code implementing a fusion-evaporation reaction process, as described in Ref. [26].

In the simulations, a key input is the ^{28}Mg initial velocity distribution which depends on the beam energy as well as the energies of the protons evaporated following formation of the compound system. The portion of the compound nucleus excitation energy given to each evaporated proton was parametrized as Gaussian distribution with a high energy exponential tail as discussed in Ref. [26]. Parameter values for the proton energy distribution were determined such that the simulated energy distribution of the 1473.59(9) keV gamma ray in ^{28}Mg agreed best with the gamma-ray lineshape observed in the thin target data in a spectrum gated on the higher-lying 2547.6(3) keV gamma ray, according to a χ^2 analysis. This method reproduces the initial velocity distribution of ^{28}Mg since the Doppler shifted energy distribution observed in the thin-target data for each TIGRESS ring depends strongly on this velocity distribution, with higher initial velocities resulting in a wider range of Doppler shifts as a function of detector angle.

Mean lifetime values for transitions observed in ^{28}Mg were determined via a comparison of experimental data and lineshapes produced using the GEANT4-based simulations using the likelihood ratio χ^2 method developed in Ref. [27] for low-statistics data. As in Ref. [27], each unique combination of a TIGRESS core and two CsI(Tl) detectors was classified into a group according to the average simulated Doppler shift factor $D = E_{\rm det}/E_0$ of a gamma ray detected in the TIGRESS core for an event containing these detectors, and lineshapes were compared to the experimental data on a group-by-group basis, as shown in Figure 3. Average Doppler shift factors contained in each group are listed in Table I. This method of grouping the data allows for clean separation of indi-

TABLE I. Listing of gamma ray/charged particle detector groups corresponding to unique TIGRESS/CsI(Tl) detector combinations with a range of average Doppler shift factors $D = E_{\rm det}/E_0$ for gamma rays detected in the TIGRESS core derived from the GEANT4-based simulations.

Group	D	No. of detector combinations
1	$1.032 < D$	6370
2	$1.018 < D \leq 1.032$	4286
3	$1.0 < D \leq 1.018$	5990
4	$0.980 < D \leq 1.0$	7330
5	$0.968 < D \leq 0.980$	3657
6	$D \leq 0.968$	6333

vidual components of the lineshape.

Transitions with no observed feeding were studied first, and their resulting effective lifetimes $\tau_{\rm eff}$ were then used as inputs to simulate feeding for lower lying transitions, as described in Ref. [26]. Feeding was observed for the first two excited states at 1473.63(9) and 4021.4(3) keV excitation energy.

The systematic uncertainty $\delta\tau_{\rm sys}$ in $\tau_{\rm mean}$ of each transition due to the stopping process was determined using the method of Ref. [26], via comparison of best-fit lifetimes obtained when using stopping tables derived from the ICRU 73 [28] and SRIM [29] models (adopted values were determined using the IRCU 73 model). Due to the low statistics obtained in the gated experimental data, the statistical uncertainty $\delta\tau_{\rm stat}$ was dominant for transitions at high excitation energy.

B. Angular distributions

Spins of observed levels were investigated using experimentally observed gamma-ray angular distributions, constructed from the number of counts observed in all TIGRESS detector cores at a fixed azimuthal angle with respect to the beam axis.

Correction of the experimental distributions for the relative detection efficiency in each of the TIGRESS rings was performed by normalizing the angular distribution of the gamma ray of interest to that of the 2754 keV gamma ray observed on a per-ring basis in beta decay data taken during beam-off periods of this experiment. This normalized angular distribution was then fitted to a Legendre polynomial series to determine the a_2 and a_4 coefficients which determine the multipolarity of the transition:

$$W(\theta) = 1 + a_2 P_2(\cos\theta) + a_4 P_4(\cos\theta). \qquad (1)$$

Tabulated values of a_2 and a_4 are shown in Table II. Fitted angular distribution data is shown in Figure 4. For some high-lying transitions with low statistics, the only information provided by the angular distribution was whether the distribution was peaked at 90° ($a_2 < 0$) or at 0° ($a_2 > 0$). In these cases, the value of a_2 with a_4 fixed to zero is also shown in Table II.

TABLE II. Table of a_2 and a_4 coefficients obtained from angular distributions of gamma-rays observed in this work.

Gamma-ray energy (keV)	a_2	a_4	$a_2(a_4 = 0)$
1163.1(4)	0.6(5)	0.1(6)	0.5(3)
2506.7(8)	0.0(4)	0.1(5)	-0.1(3)
2547.6(3)	0.20(10)	-0.19(13)	
3082.5(12)	0.7(5)	0.6(5)	
3726(2)	-0.3(6)	0.0(7)	-0.3(4)
3907.6(12)	0.2(4)	-0.3(5)	0.36(19)
4664.9(12)	-0.5(8)	-0.2(10)	-0.4(5)

Tentative spin assignments for levels in ^{28}Mg were made based on a_2 and a_4 values for gamma rays depopulating the level, level excitation energies, the observed decay scheme, and/or transition rate arguments. Furthermore, based on transition rate estimates the multipolarities of all observed transitions were assumed to be E2 or lower with the exception of the 4664.9(12) keV gamma ray depopulating the 6139.0(12) keV level as discussed below.

IV. PROPERTIES OF OBSERVED LEVELS

Several new levels and gamma rays were observed at high excitation energy near the neutron separation energy of $S_n = 8503.4(20)$ keV. The strong presence of ^{27}Mg (2p1n channel) in the unseparated data provides additional evidence that ^{28}Mg was populated at energies close to S_n in this experiment. Based on the measured gamma-ray intensities, 64(7)% of the population of the 4_1^+ state and 98(4)% of the population of the 2_1^+ state originates from observed feeding by higher lying states.

Some low-spin levels in ^{28}Mg including excited 0^+ states previously observed at 3862 and 5702 keV [19] were not observed in this experiment. This is likely because the fusion-evaporation process typically imparts significant angular momentum onto the compound system, preferentially populating levels with high spin.

Detailed results obtained for select levels of interest are provided below (in descending order of excitation energy).

A. 8438 keV level

A gamma ray at 4418 keV was tentatively observed in a previous study by Keyes *et al.* [30] in which it was tentatively assigned to a $6_1^+ \rightarrow 4_1^+$ transition from a level at 8438 keV. In this work a level is inferred at 8438(5) keV from the presence of a gamma ray at 4416(5) keV (with the uncertainty limited by statistics), confirming the previous observation. However other candidates for the yrast 6^+ state are also observed at level energies of

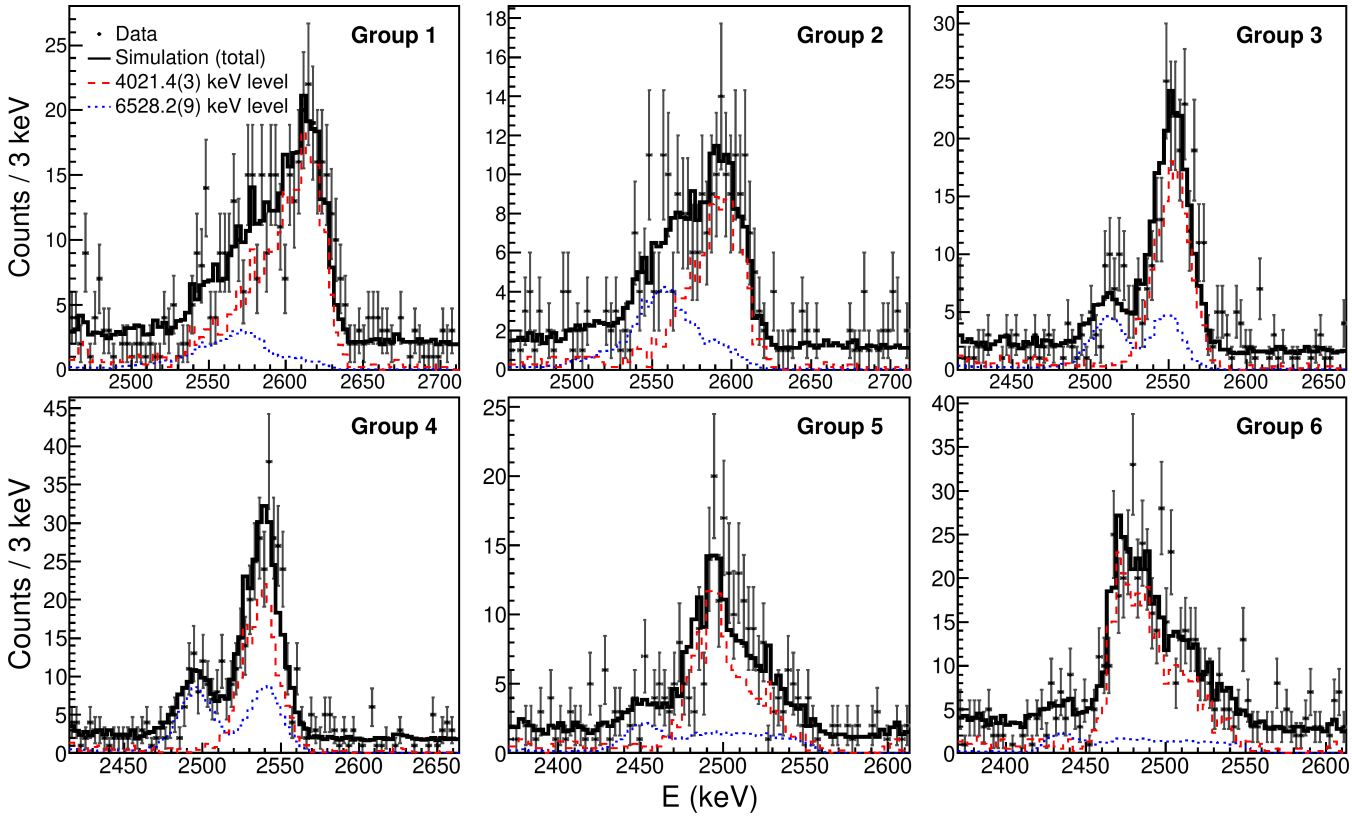

FIG. 3. Comparison of lineshapes from data and GEANT4 simulations for the gamma rays depopulating the 4021.4(3) and 6528.2(9) keV levels in ^{28}Mg, shown for each detector group. $\tau_{\rm mean}$ values of 180 fs for the 4021.4(3) keV level and 190 fs for the 6528.2(9) keV level were used. The total simulated lineshape contains contributions from the decay of both levels, as well as feeding of the 4021.4(3) keV level from the 5184.3(5) and 6528.2(9) keV levels.

7929.3(12) and 7747(2) keV. All of these levels are observed in coincidence with the $4_1^+ \rightarrow 2_1^+$ and $2_1^+ \rightarrow 0_1^+$ transitions, and lie at excitation energies in general agreement with the $I(I+1)$ level spacing predicted assuming the nucleus acts as a rigid rotor. However, the systematics and level spacing between the 2_1^+, 4_1^+ , and 6_1^+ levels in neighbouring isotopes and isotones (shown in Figure 5) suggest that the 6_1^+ level in ^{28}Mg lies below 8 MeV excitation energy, which excludes the 8438(5) keV level.

Due to insufficient statistics, the lifetime and spin-parity of the 8438(5) keV level could not be directly determined from the data. However, as there is no apparent stopped line for the 4416(5) keV gamma ray in the DSAM data, the lifetime of the level is inferred to be shorter than 1.5 ps based on comparison to the low-intensity stopped line observed for the 4664.9(12) keV gamma ray depopulating a level at 6139.0(12) keV (see Section IV F). Based on this lifetime limit, the observed transition from this level is assumed to be M2 or lower from a comparison to Weisskopf estimates. From the observed decay scheme, the spin of this level is then restricted to $I = (5, 6)$, as no transitions from this level to the known low-lying 2^+ and 3^- levels are observed. If the 8438(5) keV level were low spin, M1 and/or E2 transitions to these low-lying levels would be expected to dominate the branching.

B. 7929 keV level

A previously unobserved gamma ray at 3907.6(12) keV was assigned to a transition from a new level at 7929.3(12) keV to the 4_1^+ level in ^{28}Mg. Although this gamma ray is expected to overlap with the single-escape peak of the 4418 keV gamma ray, the intensity of the escape peak predicted from GEANT4-based simulations developed for the TIGRESS spectrometer in Ref. [26] is $< 10\%$ the intensity of the observed peak, hence a new transition was inferred.

A lifetime limit $\tau_{\rm mean} < 42$ fs was determined for this level from the lineshape simulations. Simulations were performed with both the gamma ray energy E_γ and effective lifetime $\tau_{\rm mean}$ as free parameters. The minimum χ^2 value simultaneously corresponding to the best E_γ and $\tau_{\rm mean}$ values were found by fitting the χ^2 surface in two dimensions, as shown in Fig. 6. The limit $\tau_{\rm mean} < 42$ fs was adopted based on the 90 % confidence bound of the χ^2 surface, assuming a minimum at 0 ps lifetime.

The level excitation energy of 7929.3(12) keV suggests

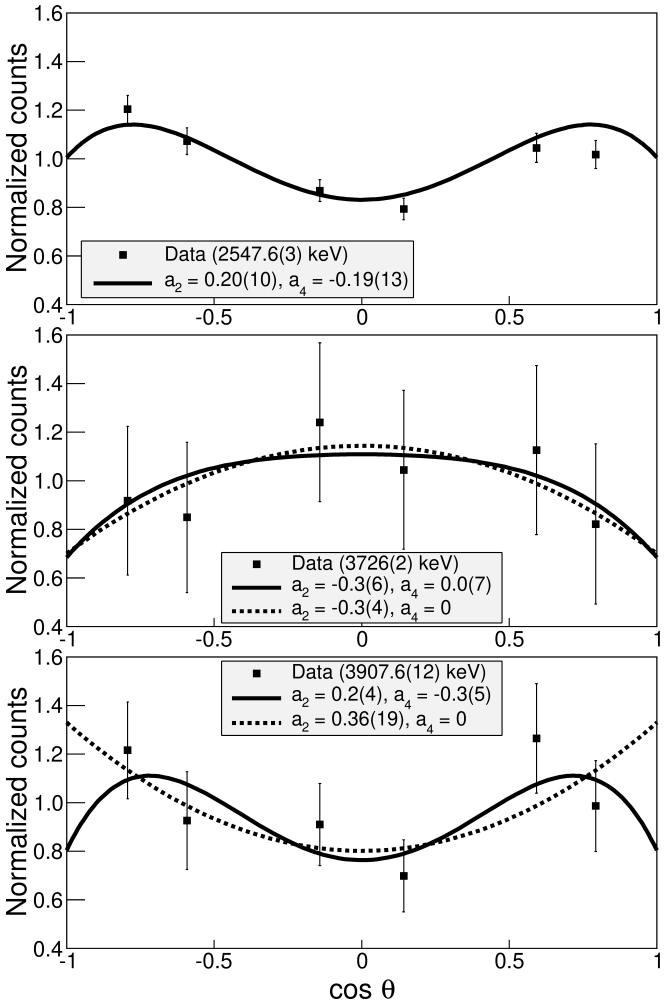

FIG. 4. Angular distributions of the 2547.6(3) keV, 3726(2) keV, and 3907.6(12) keV gamma rays observed in this work, normalized to the relative efficiency of each ring of TIGRESS cores. Fits to Equation 1 are shown.

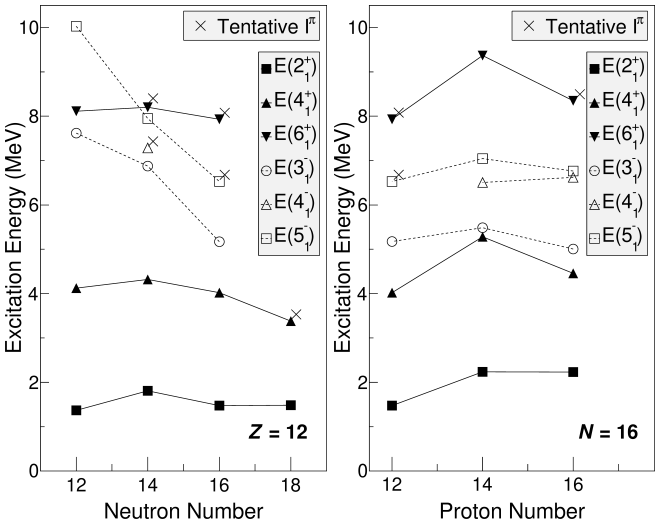

FIG. 5. Left: systematics of known yrast states in $Z = 12$ isotopes [18, 19, 31, 32]. Right: systematics of known yrast states in $N = 16$ isotones [19, 20, 33]. Levels from this work which are candidates for the 6_1^+ ($I^\pi = (6^+)$, 7929.3(12) keV) and 5_1^- ($I^\pi = (4,5)^-$, 6528.2(9) keV) levels in ^{28}Mg are shown.

that the newly observed state is a candidate for the yrast 6^+ level in ^{28}Mg. The a_2 and a_4 values determined for the angular distribution of the 3907.6(12) keV gamma ray in Table II and Figure 4, particularly the positive a_2 value, suggest that this gamma ray corresponds to an E2 transition. When measuring the angular distribution, data from the thin and thick target parts of the experiment was combined, as there were no gamma rays observed to overlap with the 3907.6(12) keV gamma ray in the ^{28}Mg data and the observed Doppler shift of this gamma ray was consistent in both sets of data due to the short lifetime of the transition.

Based on the angular distribution of the 3907.6(12) keV gamma ray, the 7929.3(12) keV level is the best candidate in this data for the yrast 6^+ state in ^{28}Mg. The case for a 6^+ assignment is further supported by the systematics of neighbouring isotopes and isotones shown in Figure 5, and the preference for population of high-spin states by the fusion-evaporation process. The 7929.3(12) keV state is therefore assigned $I^\pi = (6^+)$.

C. 7747 keV level

A previously unobserved gamma ray at 3726(2) keV was assigned to a transition from a new level at 7747(2) keV to the 4_1^+ level in ^{28}Mg. A lifetime limit $\tau_{\text{mean}} < 85$ fs was determined for this level using the GEANT4-based lineshape simulations. When gating on the $2_1^+ \rightarrow 0_1^+$ transition, the lineshape of the 3726(2) keV gamma ray overlapped with the 3698(3) keV gamma ray depopulating a level observed at 5172.9(7) keV, so the lifetimes of the two levels were determined simultaneously.

Due to its excitation energy of 7747(2) keV, this level may be considered as a candidate for the yrast 6^+ level in ^{28}Mg. When gating on the $2_1^+ \rightarrow 0_1^+$ transition, the gamma ray at 3726(2) keV overlapped with a gamma ray observed in ^{28}Mg at 3698(3) keV, so the angular distribution of this gamma ray was studied using a gate on the $4_1^+ \rightarrow 2_1^+$ transition, which removed the overlapping gamma rays but reduced statistics significantly. As shown in Table II, the a_2 and a_4 values are inconclusive, but do not favour an E2 transition (which corresponds to $a_2 > 0$). Therefore the previously discussed level at 7929.3(12) keV is a stronger candidate for the yrast 6^+ state in ^{28}Mg. Using the arguments applied to the 8438(5) keV level, it is argued that the spin of this level is greater than $4\hbar$. As the 7929.3(12) keV level was assigned $I^\pi = (6^+)$ and is assumed to be yrast (based on a comparison to the level energy systematics of Figure

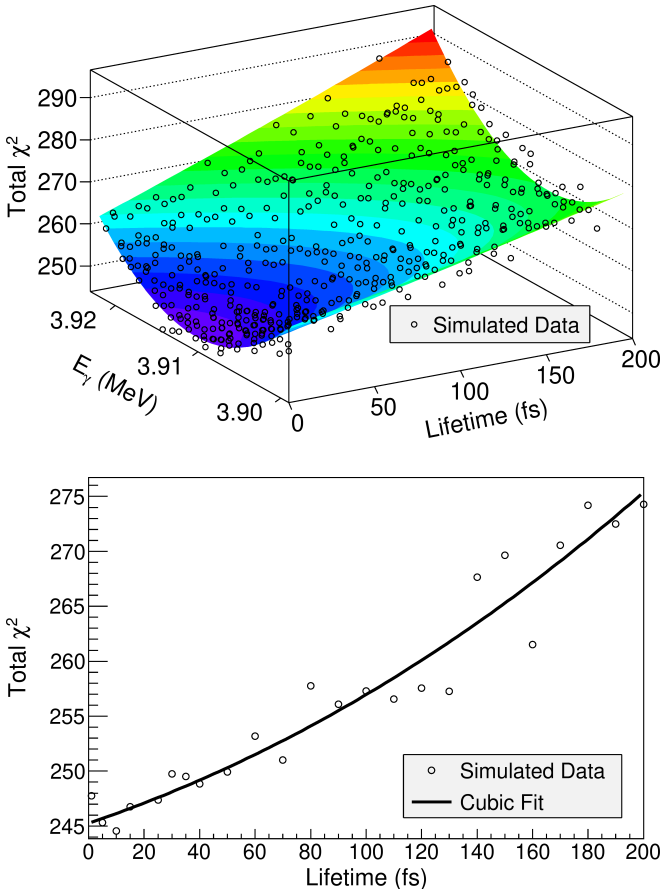

FIG. 6. Top: χ^2 surface plot in gamma ray energy and mean lifetime for the 7929.3(12) keV level in ^{28}Mg, showing a surface fit to the simulated data points. Bottom: Projection of the χ^2 surface at the fit minimum $E_\gamma = 3.911(4)$ MeV.

5), the 7747(2) keV is assigned $I = (5)$.

D. 7203 keV level

A gamma ray at 3181(3) keV was observed in coincidence with the $2_1^+ \rightarrow 0_1^+$ and $4_1^+ \rightarrow 2_1^+$ transitions and a gamma ray at 5723(5) keV in coincidence with the $2_1^+ \rightarrow 0_1^+$ transition, from which we infer the existence of a level at 7203(3) keV. Due to the large uncertainty associated with energy calibration for the 5723(5) keV gamma ray, this level energy was calculated using only the 3181(3) keV gamma ray. The possibility of the 3181(3) keV gamma ray being a single escape peak for the gamma ray at 3698(3) keV was ruled out by its observation in coincidence with the $4_1^+ \rightarrow 2_1^+$ transition. In order to accurately measure the branching of transitions depopulating the 7203(3) keV level, the contamination of a single escape peak was taken into account when determining the intensity of the 3181(3) keV gamma ray by measuring the intensity relative to that of the 1473.59(9) keV gamma ray when observed in coincidence with the $4_1^+ \rightarrow 2_1^+$ transition. After performing this correction, the intensity of the 5723(5) keV gamma ray was determined to be 27(13)% of the 3181(3) keV gamma ray.

The level energy is consistent with that of a level at 7200.3(6) keV previously observed via beta decay of ^{28}Na [9]. However the placement of gamma rays differs compared to the previous work, which does not show this level decaying to the 4_1^+ or 2_1^+ levels, indicating that the gamma rays observed in this work correspond to depopulation of a new level and that there are most likely two levels near 7.2 MeV in ^{28}Mg. The data does not rule out the possibility of the 5723(5) keV gamma ray corresponding to depopulation of a separate level close in energy to the 7203(3) keV level, however the present placement of this transition in Figure 1 has been adopted due to its consistency with the measured energy uncertainties. Additional evidence for population of a second level close in energy to 7203(3) keV, such as the presence of lower energy gamma rays depopulating such a level, has not been observed in this data.

A lifetime limit $\tau_{\text{mean}} < 380$ fs was determined for this level via the GEANT4-based simulations, using the lineshape of the 3181(3) keV gamma ray. From the lifetime and the observed decay scheme, the spin-parity of this level is assigned $I^\pi = (2^+, 3, 4^+)$ under the assumption that the multipolarity of observed transitions is E2 or lower.

E. 6528 keV level

A previously unobserved gamma ray at 2506.7(8) keV was identified in coincidence with the $2_1^+ \rightarrow 0_1^+$ and $4_1^+ \rightarrow 2_1^+$ transitions. In addition, a low-intensity gamma ray at 1356.3(12) keV was identified in coincidence with the $2_1^+ \rightarrow 0_1^+$ and $3_1^- \rightarrow 2_1^+$ transitions as shown in Figure 7. Thus the existence of a level with energy 6528.2(9) keV is inferred. This level energy agrees with that of a level previously observed at 6516(15) keV from magnetic spectrograph measurements of Ref. [34].

The 2506.7(8) keV gamma ray partially overlaps the 2547.6(3) keV gamma ray of the $4_1^+ \rightarrow 2_1^+$ transition in the thick target data. Additionally, the 2506.7(8) keV gamma ray corresponds to a transition to the 4_1^+ level at 4021.4(3) keV, such that the observed lineshape of the 2547.6(3) keV gamma ray is affected by the feeding from the 2506.7(8) keV gamma-ray transition. Due to the overlap and feeding scheme, the lifetimes of the 4021.4(3) and 6528.2(9) keV levels were determined simultaneously, by simulating lineshapes corresponding to direct population of the 4021.4(3) keV level, feeding of the 4021.4(3) keV level from the 6528.2(9) keV level, and feeding of the 4021.4(3) keV level from another level observed at 5184.3(5) keV. These branches represent all statistically significant observed feeding of the 4021.4(3) keV level. The lifetimes of both the 4021.4(3) and 6528.2(9) keV levels were varied in the simulations (the 5184.3(5) keV level lifetime was fixed based on the value determined

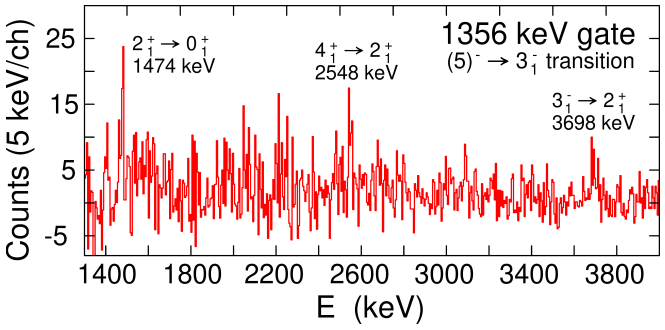

FIG. 7. Background subtracted gamma-ray coincidence spectrum following gating on the 1356.3(12) gamma ray in ^{28}Mg.

from analysis of its corresponding gamma-ray lineshape for the 1163.1(4) keV transition) and the best fit values were determined by minimizing χ^2 on a two dimensional grid with $\tau_{\rm mean}$ for the two levels as free parameters. The resulting best-fit lifetimes were $1.9(6) \times 10^2$ fs for the 6528.2(9) keV level and $1.8(3) \times 10^2$ fs for the 4021.4(3) keV level, with the corresponding lineshape fits shown in Figure 3.

The a_2 and a_4 angular distribution coefficients shown in Table II for the 2506.7(8) keV gamma ray depopulating this level were inconclusive for spin-parity assignment. Based on the observed transitions to the 3^-_1 and 4^+_1 levels, the spin of the level is assumed to be 4 or 5. A 4^+ assignment can be excluded based on non-observation of a transition to the 2^+_1 level ($E_\gamma = 5055$ keV). The intensity limit of this hypothetical transition was determined to be < 2.7 % that of the observed transition to the 4^+_1 level, which would lead to an extremely low E2 transition strength of B(E2) $< 8.39 \times 10^{-3}$ W.u. A 5^+ assignment can also be excluded since such an assignment would cause the observed transition to the 3^-_1 level to have an extremely large M2 transition strength B(M2) $= 9(3) \times 10^2$ W.u. The level is therefore assigned $I^\pi = (4, 5)^-$. Of the two values, the $I^\pi = 5^-$ case is favoured based on the systematics of 4^-_1 and 5^-_1 levels in neighbouring isotopes and isotones shown in Figure 5, since the observed level energy of 6528.2(9) keV relative to the $I^\pi = 3^-$ level at 5172.9(7) keV is consistent with the observed spacing between 5^-_1 and 3^-_1 levels in neighbouring nuclei, whereas existing experimental data is insufficient to infer such a trend for 4^-_1 levels.

F. 6139 keV level

A level at 6139.0(12) keV was identified based on observation of a gamma ray at 4664.9(12) keV in coincidence with the $2^+_1 \rightarrow 0^+_1$ transition. This level energy agrees with that of a level previously observed at 6135(15) keV from magnetic spectrograph measurements of Ref. [34]. The lineshape of the 4664.9(12) keV gamma ray shown in Figure 8 indicates that it is stopped in the DSAM target data, corresponding to a 1.0 ps lower limit for the mean lifetime of this level. When combined with the high energy of the gamma ray, a very small transition strength is implied. As shown in Figure 8, all high energy gamma rays except 4664.9(12) keV are washed out when summing the DSAM target data over Doppler shift groups, indicating that only the 4664.9(12) keV gamma ray is emitted at rest. The presence of this gamma ray in the Doppler corrected thin target data and in coincidence with the ^{28}Mg $2^+_1 \rightarrow 0^+_1$ transition indicates that the 4664.9(12) keV line belongs to ^{28}Mg and does not originate from beta decay or a contaminant reaction channel.

In addition to the lower limit on the lifetime of this level discussed prior, an upper limit may be estimated since a stopped line is not observed in the thin target data. Since the thin target has a stopper foil mounted $\sim$2 mm downstream from the target foil, the absence of a stopped line indicates that the decay occurs before the ^{28}Mg nucleus is able to traverse this distance. Assuming that the nucleus exits the target with speed $0.04c$ (based on GEANT4 simulations) and that the target-stopper separation does not exceed 3 mm, an upper limit of 250 ps is determined for the lifetime of the 6139.0(12) keV level.

The angular distribution coefficients shown in Table II for the 4664.9(12) keV gamma ray are inconclusive for spin-parity assignment, however a gamma-ray multipolarity of (M2) is assigned based on the single-particle Weisskopf estimates, which for multipolarities below M2 give lifetimes significantly lower than 1 fs at this gamma-ray energy. The (M2) assignment is further supported by existing lifetime measurements for other levels, as all high energy E1, M1 and E2 transitions in ^{28}Mg have been observed with lifetimes significantly shorter than 1 ps, implying that the observed transition is higher order than E2. Additionally, the 6139.0(12) keV level cannot be positive parity, since this would imply the existence of short-lived M1 and E2 transitions to other known positive parity states in ^{28}Mg which are ruled out by the long lifetime of the observed transition. In principle if the transition is M2 it should be out-competed by fast E1 transitions to positive parity states, however this is also ruled out by the long lifetime of the observed transition. Either there is no final state to which an E1 transition may occur, or any E1 transitions which occur are hindered in rate compared to the M2 transition. E1 transitions in ^{28}Mg have previously been shown to be hindered by a factor of $10^{-3} - 10^{-4}$ with respect to the Weisskopf estimate in the case of the 5172.9(7) keV level, as discussed in Ref. [9] and as indicated by the measured lifetime of this level in Table III. This hindrance, combined with the reduced energy of a hypothetical E1 transition compared to the observed 4664.9(12) keV (M2) transition, may explain the non-observation of competing transitions from the 6139.0(12) keV level.

An M2 assignment for the transition to the 2^+_1 level implies a spin-parity of 0^- or 4^- for the 6139.0(12) keV level. The 0^- case is favoured based on the observed de-

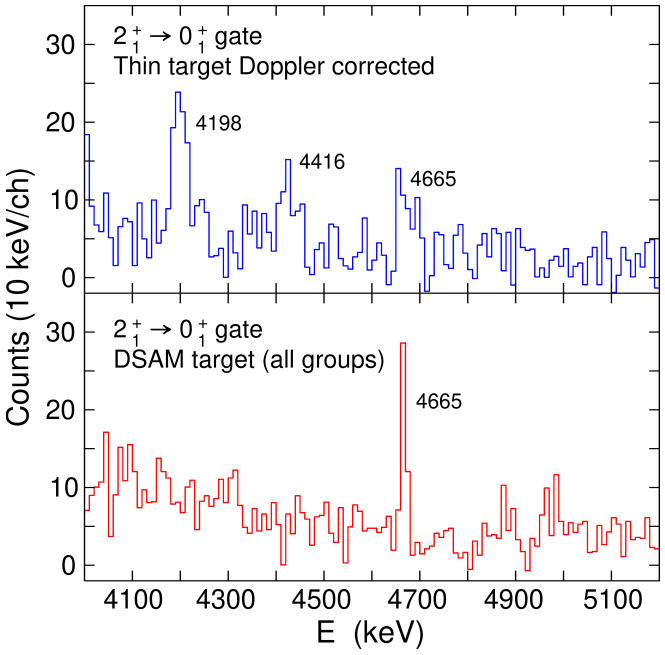

FIG. 8. Lineshape of the 4664.9(12) keV gamma ray observed in background subtracted thin target and summed DSAM target data.

cay scheme, since no transition is observed from this level to the 3_1^- level at 5172.9(7) keV. The upper limit for the intensity of a transition to the 3_1^- level was established as 11 % relative to the observed transition to the 2_1^+ level. If the spin-parity of the 6139.0(12) keV level is 4^-, this would imply a B(M1; $4^- \rightarrow 3^-$) $< 3.47 \times 10^{-3}$ W.u., corresponding to an M1 transition which would be significantly weaker than other known M1 transitions in ^{28}Mg (the weakest possible B(M1) value of the known transitions corresponds to depopulation of the 4879(2) keV level with B(M1; $2^+ \rightarrow 2_1^+$) $> 2.12 \times 10^{-2}$ W.u., using the data of Ref. [19] and the revised lifetime limit reported in Table III). However, the 4^- case cannot be fully excluded based on this evidence, as very small B(M1) values have been measured in the neighbouring isotone ^{30}Si [20]. Furthermore, the level energy of 6139.0(12) keV is consistent with the 4_1^- levels in neighbouring isotones shown in Figure 5, and preferential population of high spin states is expected using fusion-evaporation. Therefore, this level is assigned $I^\pi = (0, 4)^-$.

G. 5184 keV level

A level at 5184.3(5) keV was identified from a gamma ray at 1163.1(4) keV in coincidence with the $2_1^+ \rightarrow 0_1^+$ and $4_1^+ \rightarrow 2_1^+$ transitions. A transition from this level to the 2_1^+ level ($E_\gamma \approx 3711$ keV) was not ruled out as it may be obscured by gamma rays observed at 3698(3) and 3726(2) keV. An intensity limit $< 28\%$ was established for this hypothetical transition relative to the observed gamma ray at 1163.1(4) keV. A mean lifetime of 21^{+15}_{-14} fs was determined for the 5184.3(5) keV level based on the lineshape simulations.

The angular distribution coefficients shown in Table II are inconclusive for determining the spin-parity of this level, however the short lifetime precludes a negative parity assignment as E1 transitions are known to be hindered in ^{28}Mg based on the lifetime of the 3_1^- level. Moreover, as the decay scheme indicates strong branching to the 4_1^+ level rather than the 2_1^+ level, the spin of this level is assumed to be ≥ 4. The level energy of 5184.3(5) keV is much lower than predicted values for the yrast 5^+ and 6^+ levels from shell model calculations shown in Section VI, therefore this level is assigned $I^\pi = (4^+)$.

H. 5173 keV level

A level at 5172.9(7) keV was identified from a gamma ray at 1151.5(6) keV in coincidence with the $2_1^+ \rightarrow 0_1^+$ and $4_1^+ \rightarrow 2_1^+$ transitions and a gamma ray at 3698(3) keV in coincidence with the $2_1^+ \rightarrow 0_1^+$ transition. The level energy and gamma rays are consistent with a previously observed level at 5171.3(4) with spin-parity 3^- [19].

The intensity of the 1151.5(6) gamma ray was measured at 41±18 % the intensity of the 3698(3) keV gamma ray, in agreement with the value of 38±2 % from the evaluated data [19]. This value assumes that the geometrical coverage of the solid angle by TIGRESS detectors is sufficient to average any effects of angular distribution in the summed spectra used for analysis.

A mean lifetime of $2.6^{+1.6}_{-1.3} \times 10^2$ fs was determined for this level based on lineshape simulations for the 3698(3) keV gamma ray. When gating on the $2_1^+ \rightarrow 0_1^+$ transition, the lineshape of the 3698(3) keV gamma ray overlapped with the 3726(2) keV gamma ray depopulating the level at 7747(2) keV, so the lifetimes of the two levels were determined simultaneously. The lifetime of the 5172.9(7) keV level determined in this work is consistent with the previously evaluated value of $1.6(13) \times 10^2$ fs [19].

I. 4556 keV level

A level at 4556.3(12) keV was identified based on observation of a gamma ray at 3082.5(12) keV in coincidence with the $2_1^+ \rightarrow 0_1^+$ transition. Two levels have been previously observed in ^{28}Mg near this energy, at 4554.6(5) keV ($I^\pi = 2^+$, $E_\gamma = 3082.6(13)$ keV) and 4561.0(5) keV ($I^\pi = 1^+$, $E_\gamma = 3087.3(5)$ keV) [19]. Based on the gamma-ray energy observed in this work it is concluded that the observed level is consistent with the 4554.6(5) keV level in Ref. [19]. A lifetime limit $\tau_{\text{mean}} < 42$ fs was determined for this level via the GEANT4-based lineshape simulations.

V. SUMMARY

Figure 1 and Tables III and IV summarize the measurements performed in this work. Level energies include a correction for the recoil energy of the ^{28}Mg nucleus following gamma-ray emission. Intensities of gamma rays $I_{\gamma,rel}$ are listed relative to the intensity of the 1473.59(9) keV gamma ray. Where appropriate, 1σ statistical and systematic uncertainties $\delta\tau_{\rm stat}$ and $\delta\tau_{\rm sys}$ are listed for lifetime values. For lifetime limits, the 90% confidence bounds are reported.

VI. DISCUSSION

A. Collectivity in the yrast band

For the 4_1^+ level at 4021.4(3) keV, the present evaluated lifetime of $1.5(5) \times 10^2$ fs [19] was based on two conflicting measurements by Fintz *et al.* [13] and Fisher *et al.* [14], as summarized in Table V. This disagreement has implications for the structure of the yrast band, as the measurement of Fintz *et al.* implies increasing B(E2; $I_i \rightarrow I_i - 2$) transition strength with increasing spin - consistent with a rotational or vibrational model, while the measurement of Fisher *et al.* implies the opposite. The lifetime measured in this work agrees with that of Fisher *et al.* with a large reduction in uncertainty, indicating that collectivity is weak in the ^{28}Mg yrast band. Figure 9 shows a comparison of measured B(E2; $I_i \rightarrow I_i - 2$) values to calculations using various phenomenological models in the *sd* and *sdpf* shells, including the USDB [35], SDPF-U [11] and SDPF-MU [12] interactions. B(E2; $I_i \rightarrow I_i - 2$) values were also calculated using various *ab initio* approaches: in-medium similarity renormalization group (IM-SRG) [36] using effective interactions with $\hbar\omega = 24$ MeV, the coupled-cluster effective interaction (CCEI) [37] using 13 major harmonic oscillator shells with $\hbar\omega = 20$ MeV, as well as the symmetry-adapted no-core shell model (SA-NCSM) using the NNLOopt chiral potential [38] in 9 major harmonic oscillator shells with $\hbar\omega = 15$ MeV. For the IM-SRG and CCEI calculations, a cutoff $\Lambda_{\rm NN} = 500$ MeV was used for the chiral N3LO NN interaction and $\Lambda_{\rm 3N} = 400$ MeV was used for the chiral N2LO 3N interaction. Effective charges $e_p = 1.5e$ and $e_n = 0.5e$ were used in all calculations except the SA-NCSM which used no effective charges. Taking into account the data from Refs. [13, 14], the CCEI calculations with effective charges best reproduce the trend of observed B(E2; $I_i \rightarrow I_i - 2$) values in ^{28}Mg. For the SA-NCSM calculations, uncertainties were determined for each data point and are plotted in Figure 9, with lower and upper limits corresponding to calculations in 9 and 11 major harmonic oscillator shells respectively. Taking these uncertainties into consideration, the SA-NCSM calculations are in the best agreement with the experimentally observed B(E2; $4_1^+ \rightarrow 2_1^+$) value, and are within the limits of the other data from this study.

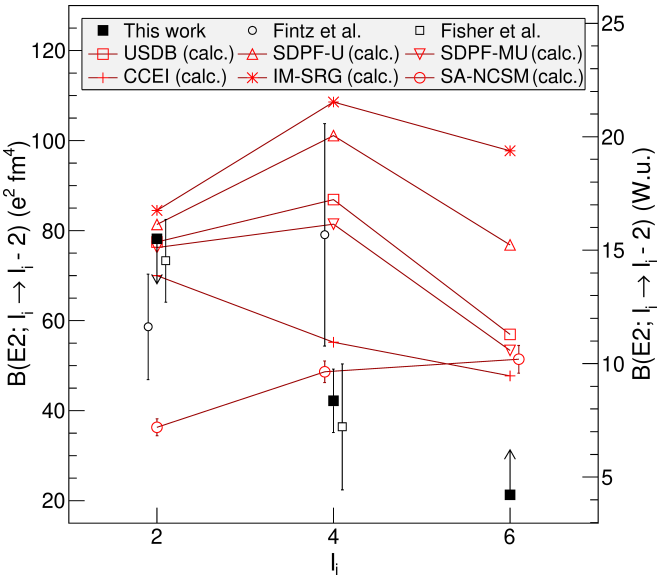

FIG. 9. Experimentally determined B(E2) values for the yrast band of ^{28}Mg, from this work and previous studies [13, 14], compared to calculated values derived from various interaction models.

Figure 10 indicates the dominant shapes in the rotational bands containing yrast and near-yrast levels calculated using the SA-NCSM. The B(E2) trend observed in the yrast band may arise from the changing contribution of these shapes as a function of spin. SA-NCSM calculations shown in Table VI indicate increased mixing between two major prolate configurations for the 4_1^+ and 6_1^+ states compared to the 0_1^+ and 2_1^+ states, which may be responsible for the hindered transition strengths from the higher lying levels. The calculated B(E2) values at high spin are lowered due to interference between terms corresponding to the mixed configurations (in the wavefunctions of the states representing the 4_1^+ and 6_1^+ levels) when calculating transition matrix elements. The contribution of the second prolate shape might be slightly enhanced by the specific interaction used, which can explain the low E2 transition strength from the 2_1^+ state seen in the calculations.

It is possible to further investigate shape deformation using the invariant sum rule analysis method of Kumar [39] and Cline [40]. Based on an invariant analysis of E2 matrix elements calculated for ^{28}Mg using the USDB interaction, the nucleus appears to exhibit some off-axial deformation, with $\delta \approx 20^\circ$ (δ is a quantity in analogy to the Bohr γ parameter, but relating to the charge distribution). The presence of this non-axial deformation appears consistent with the shape contributions to the SA-NCSM calculations summarized in Table VI.

TABLE III. List of ^{28}Mg levels and gamma rays observed in this work, and measured spin-parities and mean lifetimes compared against evaluated values from Ref. [19].

This work					Ref. [19]	
Level energy (keV)	Gamma rays (keV)	$I_{\gamma,rel}$	I^π	$\tau_{\rm mean}$ (fs)	$I^\pi_{\rm eval}$	$\tau_{\rm mean,eval}$ (fs)
1473.63(9)	1473.59(9)	1.000(15)	-	$> 1.5 \times 10^3$ [a]	2^+	$1.73(14) \times 10^3$
4021.4(3)	2547.6(3)	0.65(2)	4^+	$1.8(3) \times 10^2$	4^+	$1.5(5) \times 10^2$
4556.3(12)	3082.5(12)	0.119(16)	-	< 42 [a]	2^+	< 43
4879(2)	3405(2)	0.023(7)	-	< 26 [a]	2^+	$< 1.2 \times 10^2$
5172.9(7)	3698(3), 1151.5(6)	0.08(2), 0.031(10)	-	$2.6^{+1.6}_{-1.3} \times 10^2$	3^-	$1.6(13) \times 10^2$
5184.3(5)	1163.1(4)	0.120(9)	(4^+)	21^{+15}_{-14}	-	-
5475(3)	4001(3)	0.018(8)	-	$< 5.0 \times 10^2$ [a]	2	-
5672(3)	4198(3)	0.048(10)	-	$1.1(4) \times 10^2$	2^+	-
6139.0(12)	4664.9(12)	0.032(9)	$(0,4)^-$	$> 1.0 \times 10^3$ [a], $< 2.5 \times 10^5$ [b]	-	-
6528.2(9)	1356.3(12), 2506.7(8)	0.021(5), 0.115(12)	$(4,5)^-$	$1.9(6) \times 10^2$	-	-
7203(3)	3181(3), 5723(5)	0.033(10), 0.009(4)	$(2^+,3,4^+)$	$< 3.8 \times 10^2$ [a]	-	-
7747(2)	3726(2)	0.033(8)	(5)	< 85 [a]	-	-
7929.3(12)	3907.6(12)	0.060(11)	(6^+)	< 42 [a]	-	-
8438(5)	4416(5)	0.024(10)	(5,6)	$< 1.5 \times 10^3$ [b]	(6^+)	-

[a]Limit reported to a 90% confidence level. [b]Limit estimated based on lineshape (see text).

TABLE IV. Statistical and systematic uncertainties of $\tau_{\rm mean}$ values for ^{28}Mg levels reported in Table III. Levels with $\tau_{\rm mean}$ reported as a limit are excluded.

Level energy (keV)	$\delta\tau_{\rm stat}$ (fs)	$\delta\tau_{\rm sys}$ (fs)
4021.4(3)	20	19
5172.9(7)	$^{+130}_{-90}$	100
5184.3(5)	$^{+15}_{-14}$	2
5672(3)	40	13
6528.2(9)	50	40
7203(3)	240	50

TABLE V. Reported measurements of the mean lifetime $\tau_{\rm mean}$ of the 4^+_1 level and B(E2; $4^+_1 \rightarrow 2^+_1$) in ^{28}Mg.

Study	$\tau_{\rm mean}$ (fs)	B(E2; $4^+_1 \rightarrow 2^+_1$) (e^2fm^4)
P. Fintz *et al.* [13]	96(30)	79(25)
T. R. Fisher *et al.* [14]	210(70)	36(14)
This work	180(30)	42(7)

TABLE VI. Contributions of major triaxial and near-prolate shapes to yrast states in ^{28}Mg, based on *ab initio* SA-NCSM calculations.

I^π	triaxial $\beta = 0.18$, $\gamma = 30^\circ$	prolate $\beta = 0.16$, $\gamma = 11^\circ$	prolate $\beta = 0.16$, $\gamma = 21^\circ$
0^+_1	0.40	0.24	0.15
2^+_1	0.40	0.23	0.16
4^+_1	0.42	0.21	0.18
6^+_1	0.42	0.19	0.21

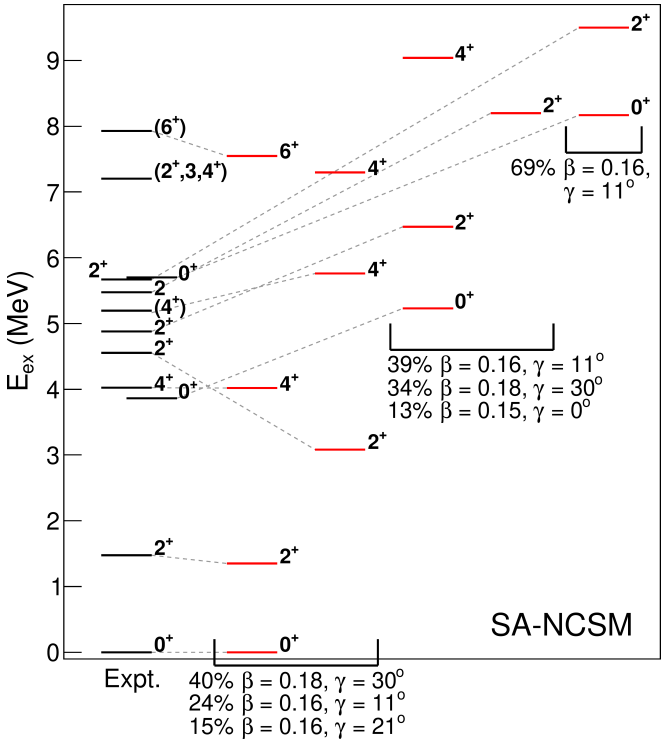

FIG. 10. Comparison of experimentally determined level energies in ^{28}Mg to calculated values derived from *ab initio* SA-NCSM calculations, with $\hbar\omega = 15$ MeV in 9 major harmonic oscillator shells. Bands are labelled based on the major shape contributions to the lowest 0^+ state, which remain roughly the same for the higher spin states (see also Table VI). Energies of excited 0^+ levels in ^{28}Mg are taken from Ref. [19], all other levels were observed in this work.

B. Influence of intruder orbitals at high excitation energy

As shown in Figure 11, calculations using the phenomenological USDB interaction [35] in the *sd* shell are able to reproduce energies of low-lying positive parity levels, in agreement with the results obtained by Kura *et al.* [9]. This result affirms the conclusion of Kura *et al.* that the low-lying levels of ^{28}Mg are dominated by *sd*-shell configurations and hence that ^{28}Mg is outside of the IoI. Furthermore, Figure 11 shows that the USDB interaction is able to reproduce level energies of high-lying levels and indicates that the $I^\pi = (5)$, (6^+) levels above 7 MeV are likely positive parity and predominantly *sd* configurations. However, the presence of levels with negative parity at high excitation energy indicates excitation of neutrons to the *pf* shell above the $N = 20$ shell gap and/or hole excitations from the *p* shell below the $N, Z = 8$ shell gap. In general, the former case might be expected due to the proximity of ^{28}Mg to the IoI. The higher spin $I^\pi = 3^-$, $(4,5)^-$ levels are more likely to contain significant population of orbitals with high total angular momentum in the *pf* shell, with $I^\pi = 5^-$ not possible from single hole excitation into the *sd* shell. The nature of the $I^\pi = (0,4)^-$ level is less clear. According to Ref. [16], $I^\pi = 0_1^-$ states in the *sd* shell are understood to transition from predominantly hole $(p - sd)$ to predominantly particle $(sd - pf)$ configurations with increasing N and Z.

To determine whether the observed negative parity states are consistent with $sd - pf$ excitations as seen in the IoI, a comparison to model calculations in the *sdpf* shell was performed utilizing the SDPF-U [11] and SDPF-MU [12] interactions. In the calculations shown in Figure 11, protons are kept in the *sd* shell while one neutron excitation to the *pf* shell is permitted. The predicted energies for negative parity states depended significantly on the interaction used, with the SDPF-MU calculations showing the best agreement with experimentally observed energy of the known 3^- levels. These calculations also show that the excitation energy of the observed $I^\pi = (4,5)^-$ level agrees well with that of the predicted 5_1^- state, and that the excitation energy of the observed $I^\pi = (0,4)^-$ level agrees very well with that of the predicted 0_1^- state. This result would suggest that the 0_1^- level in ^{28}Mg arises from a predominantly particle $(sd - pf)$ configuration. If the spin-parity of the $I^\pi = (0,4)^-$ level is instead 4^-, its wave function may be similar to that of the $I^\pi = 3^-$, $(4,5)^-$ levels, as indicated in Figure 12 which shows calculated neutron occupancies for negative parity yrast states using the SDPF-MU interaction. In these calculations the 3_1^-, 4_1^-, and 5_1^- levels are understood to arise predominantly from neutron excitation to the $f_{7/2}$ subshell, while the 0_1^- level arises instead from neutron excitation to the *p* orbitals. This prediction supports the 0^- case for the observed $I^\pi = (0,4)^-$ level, since the similar predicted neutron occupancies between the 4_1^- and 3_1^- should result in a strong M1 transition between these levels, and such a transition is not observed in the data (the branching limit for a hypothetical transition to the known $I^\pi = 3^-$ level is established in Section IV). Experimental limits for B(M1) and B(M2) values are compared to the predicted values in Table VII, indicating that the observed limits are consistent with either the 0^- or 4^- case for the SDPF-U calculations, but only with the 0^- case for the SDPF-MU calculations. The prediction of similar neutron occupancies for the 3_1^-, 4_1^-, and 5_1^- levels is further supported by the experimental data since a $(4,5)^- \to 3^-$ transition is observed.

TABLE VII. Calculated reduced transition probabilities for select transitions from the 0_1^- and 4_1^- levels, compared to experimental limits obtained for the observed $I^\pi = (0,4)^-$ level. The experimental limits for M2 transitions originate from the upper and lower bounds on the mean lifetime of the $I^\pi = (0,4)^-$ level reported in Table III and the upper bound on the intensity of the unobserved $(0,4)^- \to 3_1^-$ transition.

$\lambda L; I_i^\pi \to I_f^\pi$	$B(\lambda L, I_i \to I_f)$ (W.u.)		
	SDPF-U	SDPF-MU	Limit from expt.
M2; $0_1^- \to 2_1^+$	2.66E-1	4.04E-1	$\geq$ 7.91E-3, $\leq$ 2.19
M2; $4_1^- \to 2_1^+$	5.12E-1	5.08E-1	
M1; $4_1^- \to 3_1^-$	3.50E-4	1.82E-2	$\leq$ 3.47E-3

The $I^\pi = (0,4)^-$ level has some additional implications for the structure of ^{28}Mg. As is shown in Figure 11, there are predicted levels with $I^\pi = 1^-, 2^-$ lower in energy than the $I^\pi = 0_1^-, 4_1^-$ levels in the SDPF-U and SDPF-MU models. However, no $I^\pi = 1^-, 2^-$ levels have been firmly identified in ^{28}Mg, and no candidate levels are observed in this study, despite the possibility of strong M1 and/or E2 transitions from the $I^\pi = (0,4)^-$ level to these levels. In particular, there is a previously observed $I^\pi = 1$ level at 5193.1(5) keV which may be a candidate for the 1_1^- state [19], however that level was not observed in this work. If the 5193.1(5) keV level is $I^\pi = 1^-$, a strong $0^- \to 1^-$ M1 transition may be expected, and the absence of this transition in the experimental data may indicate that the $I^\pi = (0,4)^-$ level is 4^-. However, if the 5193.1(5) keV level is $I^\pi = 1^+$, then it is consistent with the 0^- case for the $I^\pi = (0,4)^-$ level, due to the hindrance of observed E1 transitions in ^{28}Mg. Overall, these ambiguities may be resolved in future experiments by firm assignment of the spin-parity of the levels in question (obtainable via high statistics gamma-ray angular distribution measurements and/or improved branching ratio limit measurements).

Effective single particle energies for protons and neutrons in the SDPF-MU interaction are shown in Figure 13. These calculations indicate that the $N = 20$ shell gap is significantly smaller for neutrons than for protons, supporting the claim that the lowest lying negative parity states arise from neutron excitation.

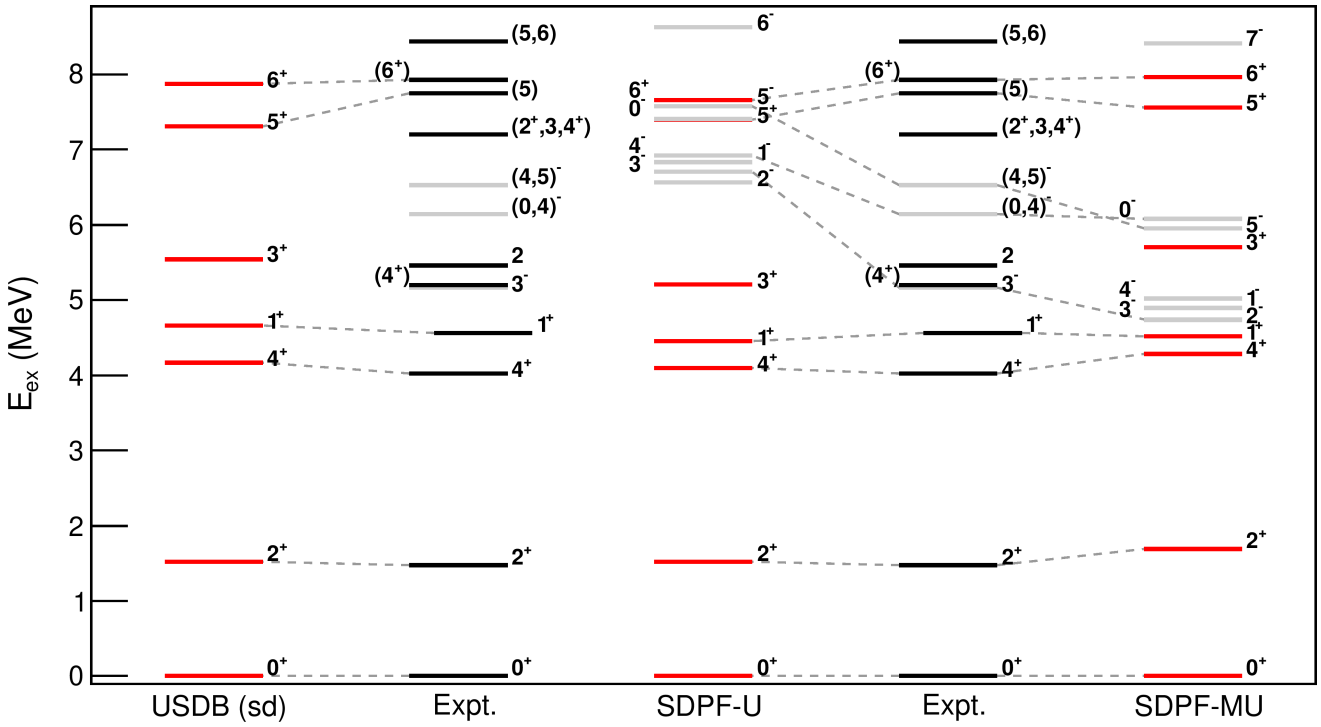

FIG. 11. Comparison of experimentally determined yrast level energies in ^{28}Mg to calculated values derived from shell models in *sd* and *sdpf* valence spaces. Connections are drawn between calculated levels and their closest candidates in the experimental data. Negative parity levels are denoted in light grey. The known $I^\pi = 1^+$ level in ^{28}Mg is taken from Ref. [19], all other levels were observed in this work. The observed $I^\pi = 3^-, (4^+)$ levels near 5.2 MeV are slightly offset in energy for readability.

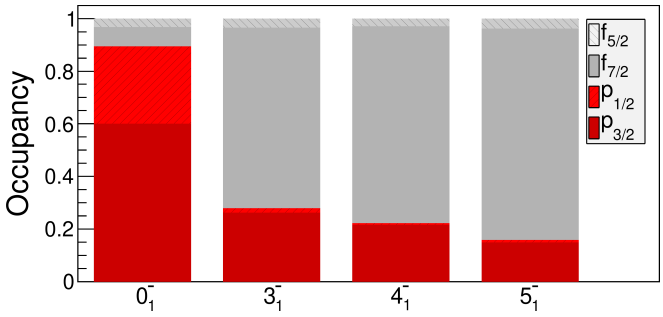

FIG. 12. Calculated neutron occupancies in the *pf* shell using the SDPF-MU interaction.

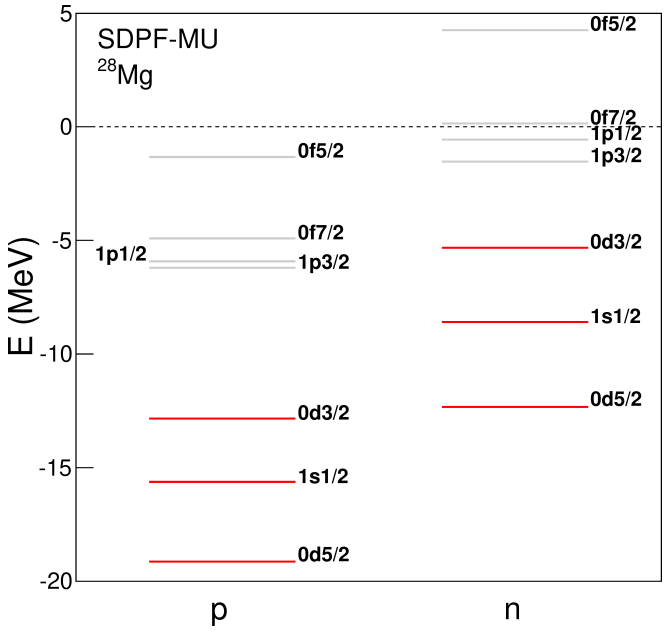

FIG. 13. Proton and neutron effective single particle energies for ^{28}Mg from the SDPF-MU interaction, with intruder orbitals denoted in light grey.

VII. CONCLUSIONS

Level energies and transition strengths have been studied in ^{28}Mg using $\gamma - \gamma$ coincidence spectroscopy and Doppler shift lifetime measurements. ^{28}Mg was populated up to its neutron separation energy using fusion-evaporation, allowing for study of previously unobserved levels at high spin. Three new levels were identified at 7203(3) keV, 7747(2) keV, and 7929.3(12) keV based on the coincidence spectroscopy. Comparison of transition strengths measured via the DSAM and the observed

branching ratios to the branching predicted using Weisskopf estimates allowed for tentative spin-parity assignments for most observed levels, including two new assignments with negative parity.

The revised B(E2; $4_1^+ \rightarrow 2_1^+$) value for ^{28}Mg obtained in this study indicates reduced collectivity in the yrast band compared to the previous results of Fintz *et al.* but in agreement with Fisher *et al.* The experimentally obtained B(E2) values in the yrast band are well reproduced by *ab initio* SA-NCSM calculations without the use of effective charges. Based on these calculations it is speculated that the reduction in collectivity which is observed at high spin results from increased mixing of two prolate deformations. The SA-NCSM is a no-core shell model with a new feature, the symmetry-adapted basis, that allows the theory to describe *sd*-shell nuclei and to include physically relevant configurations, namely, configurations in the low-lying major shells and selected configurations in higher major shells necessary to describe enhanced deformation and B(E2) values. The SA-NCSM with the chiral NNLO$_{\rm opt}$ interaction has been shown here to naturally describe collectivity in addition to the mixing of the *sd* and *pf* (and higher) shells. Large-scale calculations for neighbouring Mg isotopes will be important to provide further insight into the IoI physics.

Comparison of the experimental level energies to model calculations in the *sd* and *sdpf* shells indicates that the positive parity levels of ^{28}Mg are dominated by *sd* configurations while at high excitation energy the influence of the *pf* shell is significant. Calculations using the SDPF-MU interaction are able to reproduce the observed negative parity states by single neutron excitation into to *pf* shell. Based on these calculations, the predicted 0_1^- level in ^{28}Mg is understood to arise predominantly from neutron excitation to the *p* orbital, with other negative parity states resulting predominantly from neutron excitation to the *f* orbital.

The spin-parity assignments for high-lying levels, while supported by the observed decay scheme and model calculations, could not be conclusively determined in this work and may be an area of interest for future studies. Similar ambiguities exist in the data for other Na and Mg isotopes in this region. Future studies of shell evolution and nuclear structure near the $N = 20$ IoI may wish to investigate electromagnetic transition rates and confirmation of spin-parity assignments, as these represent some of the larger gaps in the existing data.

ACKNOWLEDGMENTS

The authors acknowledge the support of the ISAC Operations Group at TRIUMF, and the Simon Fraser University Electronics and Machine Shops. This work was supported by the Natural Sciences and Engineering Research Council of Canada. TRIUMF receives federal funding through a contribution agreement with the National Research Council of Canada.

This work was supported in part by the U.S. National Science Foundation (OIA-1738287, ACI -1713690); it benefited from computing resources provided by Blue Waters, LSU (`www.hpc.lsu.edu`), and the National Energy Research Scientific Computing Center (NERSC).

[1] B. A. Brown, Physics **3**, 104 (2010).
[2] E. K. Warburton, J. A. Becker, and B. A. Brown, Physical Review C **41**, 1147 (1990).
[3] Y. Utsuno, T. Otsuka, T. Mizusaki, and M. Honma, Physical Review C **60**, 054315 (1999).
[4] E. Caurier, F. Nowacki, and A. Poves, Physical Review C **90**, 014302 (2014).
[5] G. L. Wilson *et al.*, Physics Letters B **759**, 417 (2016).
[6] J. R. Terry, B. A. Brown, C. M. Campbell, J. M. Cook, A. D. Davies, D. C. Dinca, A. Gade, T. Glasmacher, P. G. Hansen, *et al.*, Physical Review C **77**, 014316 (2008).
[7] B. Fernández-Domínguez *et al.*, Physics Letters B **779**, 124 (2018).
[8] A. Matta, W. N. Catford, N. A. Orr, J. Henderson, P. Ruotsalainen, G. Hackman, A. B. Garnsworthy, F. Delaunay, R. Wilkinson, *et al.*, Physical Review C **99**, 044320 (2019).
[9] K. Kura, K. Tajiri, T. Shimoda, A. Odahara, T. Hori, M. Kazato, T. Masue, M. Suga, A. Takashima, *et al.*, Physical Review C **85**, 034310 (2012).
[10] K. D. Launey, T. Dytrych, and J. P. Draayer, Progress in Particle and Nuclear Physics **89**, 101 (2016).
[11] F. Nowacki and A. Poves, Physical Review C **79**, 014310 (2009).
[12] Y. Utsuno, T. Otsuka, B. A. Brown, M. Honma, T. Mizusaki, and N. Shimizu, Physical Review C **86**, 051301(R) (2012).
[13] P. Fintz *et al.*, Nuclear Physics A **197**, 423 (1972).
[14] T. R. Fisher *et al.*, Physical Review C **7**, 1878 (1973).
[15] B. Rastegar, G. Guillaume, P. Fintz, and A.Gallmann, Nuclear Physics A **225**, 80 (1974).
[16] M. Bouhelal, N. Saidane, S. Belaid, and F. Haas, Canadian Journal of Physics **96**, 774 (2018).
[17] K. W. Allen, *The Electromagnetic Interaction in Nuclear Spectroscopy* (North-Holland Publishing Company, 1975) pp. 311–339.
[18] M. S. Basunia and A. M. Hurst, Nuclear Data Sheets **134**, 1 (2016).
[19] M. S. Basunia, Nuclear Data Sheets **114**, 1189 (2013).
[20] M. S. Basunia, Nuclear Data Sheets **111**, 2331 (2010).
[21] R. E. Laxdal, Nuclear Instruments and Methods in Physics Research Section B **204**, 400 (2003).
[22] G. Hackman and C. E. Svensson, Hyperfine Interactions **225**, 241 (2014).
[23] P. Voss *et al.*, Nuclear Instruments and Methods in Physics Research Section A **746**, 87 (2014).
[24] J. Greene, P. Voss, and K. Starosta, Journal of Radioanalytical and Nuclear Chemistry **299**, 1121 (2014).
[25] `http://www.micromatter.com/`, Accessed: April 12, 2018.

[26] J. Williams *et al.*, Nuclear Instruments and Methods in Physics Research Section A **859**, 8 (2017).
[27] A. Chester *et al.*, Nuclear Instruments and Methods in Physics Research Section A **882**, 69 (2018).
[28] ICRU Report 73, Journal of the ICRU **5**, 1 (2005).
[29] J. F. Ziegler, M. D. Ziegler, and J. P. Biersack, Nuclear Instruments and Methods in Physics Research Section B **268**, 1818 (2010).
[30] K. L. Keyes *et al.*, Journal of Physics G: Nuclear and Particle Physics **31**, S1903 (2005).
[31] M. S. Basunia, Nuclear Data Sheets **127**, 69 (2015).
[32] R. B. Firestone, Nuclear Data Sheets **108**, 2319 (2007).
[33] C. Ouellet and B. Singh, Nuclear Data Sheets **112**, 2199 (2011).
[34] S. Hinds, H. Marchant, and R. Middleton, Proceedings of the Physical Society **78**, 473 (1961).
[35] B. A. Brown and W. A. Richter, Physical Review C **74**, 034315 (2006).
[36] S. R. Stroberg, H. Hergert, J. D. Holt, S. K. Bogner, and A. Schwenk, Physical Review C **93**, 051301(R) (2016).
[37] G. R. Jansen, M. D. Schuster, A. Signoracci, G. Hagen, , and P. Navrátil, Physical Review C **94**, 011301(R) (2016).
[38] A. Ekström, G. Baardsen, C. Forssén, G. Hagen, M. Hjorth-Jensen, G. R. Jansen, R. Machleidt, W. Nazarewicz, *et al.*, Phys. Rev. Lett. **110**, 192502 (2013).
[39] K. Kumar, Physical Review Letters **28**, 249 (1972).
[40] D. Cline, Annual Review of Nuclear and Particle Science **36**, 683 (1986).